Applied Mathematical Modelling 77 (2020) 1310–1330

Contents lists available at ScienceDirect

Applied Mathematical Modelling

journal homepage: www.elsevier.com/locate/apm

Numerical modelling of melt-conditioned direct-chill casting

G.S. Bruno Lebon[a,*], Hu-Tian Li[a,b], Jayesh B. Patel[a], Hamid Assadi[a], Zhongyun Fan[a]

[a] Brunel Centre for Advanced Solidification Technology, Brunel University London, Uxbridge UB8 3PH, United Kingdom
[b] Chinalco Materials Application Research Institute Co. Ltd, Beijing, PR China

ARTICLE INFO

Article history:
Received 9 January 2019
Revised 9 August 2019
Accepted 20 August 2019
Available online 27 August 2019

Keywords:
High-shear melt conditioning
Aluminium alloy
Computational fluid dynamics
Process modelling

ABSTRACT

Melt conditioned direct-chill (MC-DC) casting is a novel technology which combines direct-chill (DC) casting with a high shear device directly immersed in the sump for in situ microstructural control. A numerical model of melt-conditioned direct-chill casting (MC-DC) is presented in this paper. This model is based on a finite volume continuum model using a moving reference frame (MRF) to enforce fluid rotation inside the rotor-stator region and is numerically stable within the range of processing conditions. The boundary conditions for the heat transfer include the effects of the hot-top, the aluminium mould, and the direct chill. This model is applied to the casting of two alloys: aluminium-based A6060 and magnesium-based AZ31. Results show that MC-DC casting modifies the temperature profile in the sump, resulting in a larger temperature gradient at the solidification front and a shorter local solidification time. The increased heat extraction rate due to forced convection in the sump is expected to contribute to a finer, more uniform grain structure in the as-cast billet.

1. Introduction

Direct-chill (DC) casting is a semi-continuous casting method that produces feedstock of wrought aluminium and magnesium alloys suitable for subsequent processing, such as extrusion, rolling or forging. In DC casting, melt is poured into an open-ended, water-cooled mould with the bottom closed by a starting block. A shell is formed upon contact with the mould (primary cooling). The starting block is then pulled downwards at a specified casting speed. A water jet cools the surface of the shell when it exits the mould (secondary cooling). The billet is pulled at the casting speed to the required length while melt is continuously poured in the mould at a rate that keeps the melt level in the hot top constant [1].

A fine and uniform microstructure is desirable for DC-casting billets. Beneficial effects include enhanced mechanical properties and improved extrudability, machinability, and surface finish for downstream processing [2]. Melt-conditioned direct-chill (MC-DC) casting significantly refines the grain size of aluminium and magnesium alloys without the need for adding grain refiners [3,4]. This beneficial effect is attributed to the increase in potential nucleation sites upon deagglomeration of existing inclusions (e.g. native MgO particles in magnesium alloys) [4]. In MC-DC casting, a rotor-stator mechanism (the high shear device) is immersed into the sump. The rotor rotates at high speed in a cylindrical stator comprising many small

* Corresponding author.
E-mail address: bruno.lebon@brunel.ac.uk (G.S.B. Lebon).

https://doi.org/10.1016/j.apm.2019.08.032

Nomenclature

A	crystal constant
$\boldsymbol{A}_f$	face area vector (m^2)
C_α	phase interface compression strength parameter (dimensionless)
C_k	LES coefficient (0.094, dimensionless)
C_e	LES coefficient (1.048, dimensionless)
C^s	concentration of species s
C_0^s	initial concentration of species s
C_l^s	liquid concentration of species s
C_{sf}	nucleate boiling constant
$\boldsymbol{D}$	strain rate tensor (m s^{-1})
D_l^s	diffusivity of species s
F_μ	switching function
K	specific kinetic energy (J kg^{-1})
K_p	mushy region momentum sink coefficient (s^{-1})
L_f	latent heat of fusion (J kg^{-1})
L_v	latent heat of vaporization (J kg^{-1})
N	rotor rotation speed (s^{-1})
P	power dissipated by mixer (W)
T	temperature (K)
T_l	liquidus temperature (K)
T_s	solidus temperature (K)
T_c	coherency temperature (K)
T_{sat}	saturation temperature (K)
T_{water}	water film temperature (K)
c_p	specific heat capacity (J kg^{-1} K^{-1})
f_l	liquid volume fraction (dimensionless)
$\boldsymbol{g}$	acceleration due to gravity (m s^{-2})
g_c	packing fraction
h	enthalpy (J K^{-1})
h_q	heat transfer coefficient (W m^{-2} K^{-1})
k	turbulent kinetic energy (m^2 s^{-2})
k_p	binary partition coefficient
p	pressure (Pa)
$\boldsymbol{u}$	velocity (m s^{-1})
t	time (s)
Δ	length scale (m)
Γ	water flow rate per unit circumference (m^2 s^{-1})
Ω	under-relaxation factor
β_s	solutal expansion coefficient for species s
β_T	thermal expansion coefficient
α_l	liquid volume fraction (dimensionless)
ε	dissipation rate of turbulent kinetic energy (m^2 s^{-3})
ϕ_f	volume flux through face f(m^3 s^{-1})
μ	dynamic viscosity (Pa s)
ρ	density (kg m^{-3})
κ	thermal conductivity (W m^{-1} K^{-1})
σ	surface tension (N m^{-1})
ν	kinematic viscosity (m^2 s^{-1})
$\boldsymbol{\tau}$	subgrid scale stress (Pa)
$\boldsymbol{\omega}$	angular velocity (rad s^{-1})

holes (radial holes). The high shear rate is due to the high speed of the rotor and the small clearance between the stator and the rotor [5].

The negative pressure that is generated by the rotor blades pumps the melt upwards and forces flow out of the stator holes. As a result, a turbulent flow with high shear rate is generated in the rotor-stator mixer [5]. The advantage of MC-DC casting is that it provides both dispersive and distributive mixing in the sump, while keeping the melt surface relatively stable, thus preventing entrainment of oxides or, in the case of aluminium, absorption of hydrogen [3]. In a tank, the region

of intense mixing around the mixer is toroidal [6] and is denoted as a pseudo-cavern by the literature [7], with the region of intense mixing surrounded by stagnant fluid. The small volume of melt surrounding the mixer in a DC casting mould results in large mixing within the top portion of the sump [5].

The grain refining effect is pronounced in magnesium alloys, with pre-nucleation occurring on dispersed native magnesium oxide particles. The grain refining effect of MC-DC is presumed to be due to *explosive grain initiation* [8]: numerous solid inclusions initiate grains at the same time, with the latent heat released by the initial free growth stifling further grain initiation. Intensive melt shearing breaks down existing inclusions and disperses them as potential nucleation sites, thereby increasing the number of grains in the treated billet. A theoretical model confirmed that shearing can increase the MgO particle number density in AZ91 alloy by three orders of magnitude from 10^{14} m^{-3} to 10^{17} m^{-3}, thus enhancing heterogeneous nucleation [4]. Shearing of molten aluminium alloy prior to solidification also results in a fine equiaxed grain structure [9]. While this technology has been studied for the past few years, a systematic study of the process has yet to be conducted, especially for optimizing the process against design parameters.

Simplified numerical models of DC casting are based on the continuum model, e.g. Bennon and Incropera [10]. Vreeman et al. included the transport of solute-depleted, free floating dendrites to model DC casting of aluminium-based alloy billets [11–13]. Williams et al. used the continuum model coupled with finite element analysis to study stress deformation on ingots during the start-up phase of DC casting [14]. If a continuum model is not used, it is necessary to track the interface between the phases. Many multiphase models of DC casting are based on the model of Ni and Beckermann [15]. More refined models incorporating grain motion are derived from this approach [16,17].

A critical component of DC casting simulations is the prescription of boundary conditions. Air-gap models for primary cooling have been studied in the literature [18,19]. However, the sump profile is primarily influenced by the secondary cooling [20]. Heat transfer coefficients can be estimated using a non-dimensional relationship for a turbulent free-falling film of water taking into account the effect of nucleate boiling [21], or by calculating them from temperature measurements corresponding to the case being studied [13].

Numerical modelling has also been used to study flow features of rotor-stator mixers [22–24]. Of particular relevance is the work of Tong et al. who studied the key flow features of the high-shear device in molten aluminium alloy [5]. High shear rate was found to be confined to the close vicinity of the rotor-stator mixer and the authors concluded that effective dispersion of oxides occurred only near the mixing head [5]. Their model did not include solidification, but only melt flow.

Modification of the sump profile in DC casting due to external fields has also been studied in the literature. Lebon et al. [25] predicted acoustic streaming in the sump of a DC casting mould of the same geometry as that studied in this manuscript using a novel acoustic model that takes into account the effect of cavitating bubbles. Acoustic streaming, caused by the acoustic pressure gradient in the melt, modifies the flow pattern. This model was indirectly validated against grain morphology in different locations of the cast billet and successfully explained the resulting grain morphology modification due to the predicted flow pattern.

Another method for modifying the sump is through the application of low frequency electromagnetic (EM) fields of the order of 10 Hz. Here, the Lorentz force modifies the flow pattern. Le et al. [26] computed the flow pattern and temperature fields of DC casting of magnesium alloys under the influence of EM fields using the Finite Element Method (FEM) and determined that the sump is shallower in the presence of EM due to the increased convective heat transfer in the sump caused by the presence of additional vortices. Zhang et al. [27] coupled the FEM method for solving the EM equations and the Finite Volume Method (FVM) to solve the fluid flow and heat transfer equations. They predicted a shallower, raised sump as a result of the EM stirring and obtained a decent comparison with temperature measurements. Recent advances in Low Frequency Electromagnetic Casting (LEFC) modelling include the use of meshless methods that avoid the use of polygonal element meshes [28].

The increased heat extraction rate due to forced convection results in a more refined and uniform grain structure. In conventional DC casting, the variation of cooling rate along the radius of the billet results in a variation in grain size across the billet section. In MC-DC, the grain size across the billet cross section is harmonized [29]. Forced convection results in a larger cooling rate in the liquid-solid phase region due to the enhanced mass transfer and heat extraction rate. Combined with enhanced nucleation by dispersed oxide particles and dendrite fragmentation, melt conditioning in DC casting yields a more uniform and refined grain structure across a billet section.

In this paper, a continuum model for DC casting is solved by extending the OpenFOAM library [30] to mushy zone problems. The compiled applications are used to study the DC casting of A6060 Al-alloy and AZ31 Mg-alloy for which some experimental data is available. The model is then applied to high-shear treatment of the sump during the casting of these alloys using a rotor-stator mixer.

2. MC-DC model and governing equations

2.1. Geometry of MC-DC model

Fig. 1 illustrates the MC-DC casting process. A more detailed description of high shear melt conditioning as applied to DC casting can be found elsewhere [3,31]. The three-dimensional features of the rotor-stator mixer head is shown in Fig. 2. When the rotor blades rotate at high speed, the melt enters through the bottom opening of the stator and is ejected at high

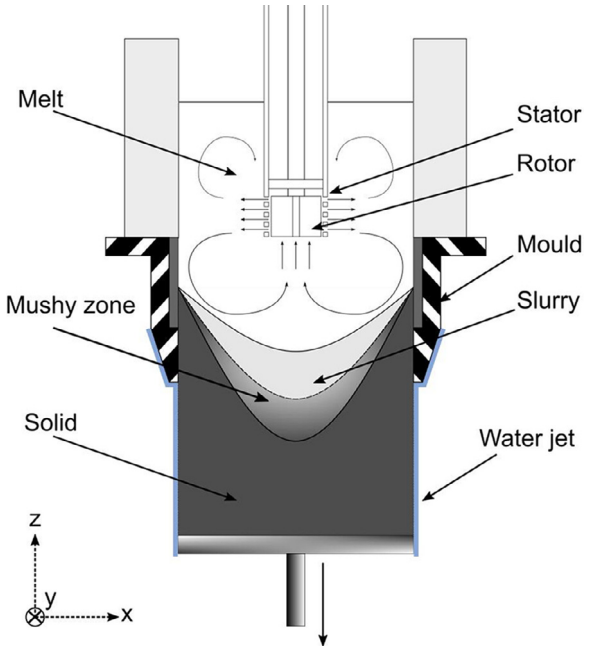

Fig. 1. Schematic diagram of the melt-conditioned direct-chill casting process. A rotor-stator mixer is immersed in the sump of a conventional DC casting setup. $\boldsymbol{x} = 0$ mm coincides with the axis of the billet and the bottom of the mixer is located at $\boldsymbol{z} = 0$ mm. The $\boldsymbol{y}$ axis is into the plane of the paper.

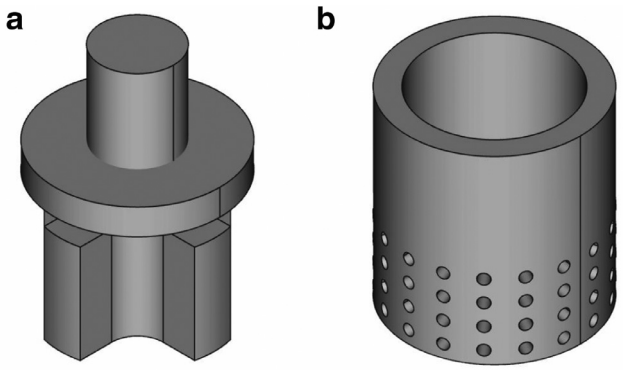

Fig. 2. (a) Rotor and (b) Stator.

speed through the holes. A stopper prevents the melt from going up the shaft. The key dimensions of the rotor and stator are available elsewhere [32]. The stator consists of 4 rows of 18 equi-spaced holes, each of diameter 2.5 mm.

The DC caster for A6060 consists of a mould of diameter 155 mm. The hot top depth in the model is set to 50 mm. Due to temperature stratification in the sump [20], the inlet temperature can be fixed to the liquidus temperature of the melt if the feeding is not modelled explicitly. The graphite ring depth is 40 mm. The aluminium mould depth is 17 mm. The water jet flows at a rate of 180 L/min at a temperature of around 20 °C. AZ31 is cast in a similar geometry, albeit with a smaller mould diameter of 80 mm.

2.2. Governing equations

A single region formulation that is derived from conservation of mass, momentum, energy, and species is used to represent this problem [11]. The continuum formulation provides realistic predictions of transport behaviour for phase change problems. This formulation avoids the difficulty in tracking phase interfaces [10], while also providing sensible results at low computational cost, a desirable feature in optimization studies.

The mass conversation equation is given by

$$\frac{\partial \rho}{\partial t} + \nabla \cdot (\rho \boldsymbol{u}) = 0, \tag{1}$$

where ρ is the melt density and $\boldsymbol{u}$ is the melt velocity.

Although a steady-state solution is expected in DC casting problems, transient equations are used in this study as the transient terms act as inertial relaxation terms that aid convergence. The solution is stopped once a stable sump profile, as indicated by the coherency isosurface, is achieved.

The energy conservation equation is given by

$$\frac{\partial(\rho h)}{\partial t} + \nabla\cdot(\rho \boldsymbol{u} h) = \nabla\cdot\{(\kappa+\kappa_t)\nabla T\} - L_f\left[\frac{\partial(\rho f_l)}{\partial t} + \nabla\cdot(\rho \boldsymbol{u} f_l)\right], \tag{2}$$

where $h = c_p T$ is enthalpy, κ is thermal conductivity, $\kappa_t = c_p \alpha_t$ is the turbulent thermal conductivity, T is temperature, c_p is specific heat capacity, L_f is latent heat of fusion, and f_l is the volume fraction of liquid. The last term is the energy associated with phase change [33,34]. α_t is the effective thermal turbulent diffusivity and is calculated from the kinematic turbulent viscosity ν_t as $\alpha_t = \rho\nu_t/\mathrm{Pr}_t$. Pr_t is the turbulent Prandtl number and is set to 1.0. The liquid fraction is calculated from the National Physical Laboratory's Virtual Measurement Systems (VMS) [35,36] assuming Scheil solidification and is implemented in the model using a temperature lookup table.

The species conservation equation is given by

$$\frac{\partial(\rho C^s)}{\partial t} + \nabla\cdot(\rho \boldsymbol{u} C^s) = \nabla\cdot\left(\rho f_l D_l^s \nabla C^s\right) + \nabla\cdot\left\{\rho f_l D_l^s \nabla\left(C_l^s - C^s\right)\right\} - \nabla\cdot\left\{\rho(\boldsymbol{u}-\boldsymbol{u}_s)\left(C_l^s - C^s\right)\right\}, \tag{3}$$

where C^s is the concentration of species s, and D_l^s is the diffusivity of species s in the liquid. The liquid concentration is calculated using the lever rule

$$C_l^s = C^s/\{(1-f_l)k_p + f_l\}, \tag{4}$$

where k_p is a binary partition coefficient.

Above a packing fraction g_c, free-floating dendrites coalesce and form a rigid dendritic structure. This fraction divides the phase transition zone into a slurry zone and a mushy zone. The momentum conservation equation in the liquid and slurry regions is given by

$$\frac{\partial(\rho \boldsymbol{u})}{\partial t} + \nabla\cdot(\rho \boldsymbol{u}\boldsymbol{u}) = \nabla\cdot\{(\mu+\mu_t)\nabla \boldsymbol{u}\} - \nabla p + \rho_b \boldsymbol{g}, \tag{5}$$

where μ is the dynamic viscosity, μ_t is the turbulent viscosity, p is pressure, and $\boldsymbol{g}$ is the acceleration due to gravity. The buoyancy term is evaluated in assuming the Boussinesq approximation, i.e.

$$\rho_b \boldsymbol{g} = \rho_{ref}\boldsymbol{g}\left[\beta_T\left(T - T_{ref}\right) - \sum_s \beta_s\left(C_l^s - C_0^s\right)\right], \tag{6}$$

where β_T is the thermal expansion coefficient and β_s is the solute expansion coefficient for species s. C_0^s is the reference concentration value for species s.

In the slurry region, the viscosity is modified to simulate flow with resistance due to the presence of grains

$$\mu_{l,m} = \mu_l \Big/ \left\{1 - F_\mu \frac{(1-f_l)}{A}\right\}^2, \tag{7}$$

where F_μ is a switching function and A is a crystal constant [37].

In the mushy zone and solid regions, the momentum conservation equation is given by

$$\frac{\partial(\rho \boldsymbol{u})}{\partial t} + \nabla\cdot(\rho \boldsymbol{u}\boldsymbol{u}) = \nabla\cdot\{(\mu+\mu_t)\nabla \boldsymbol{u}\} - \nabla p + \rho_b \boldsymbol{g} - (\boldsymbol{u}-\boldsymbol{u}_s)\frac{\left(1-f_l^2\right)}{f_l^3}K_p, \tag{8}$$

where $\boldsymbol{u}_s$ is the velocity of the solid shell which is set as the casting speed, and K_p is the permeability coefficient. The last term of Eq. (8) is a Carman–Kozeny source term that accounts for the resistance to flow in the mushy/solid region. The expression $(\boldsymbol{u}-\boldsymbol{u}_s)$ ensures that the solid material moves as a bulk at the casting speed [33,34].

Using a moving reference frame (MRF), rotation at angular velocity $\boldsymbol{\omega}$ is implemented by using relative velocities for the convective flux, i.e.

$$\nabla\cdot(\rho \boldsymbol{u}\boldsymbol{u}) = \nabla\cdot(\rho \boldsymbol{u}_{rel}\boldsymbol{u}) + \rho(\boldsymbol{\omega}\times\boldsymbol{u}), \tag{9}$$

where $\boldsymbol{u}_{rel}$ is velocity relative to the rotating frame. While the evaluation of the flow pattern using a moving mesh, or adaptive mesh interface (AMI), results in more accurate results, this method places a large restriction on the time step. Using AMI, time steps should be chosen in such a way that the sliding mesh perfectly overlaps the non-rotating mesh to reduce interpolation errors. Also, a maximum of 3° turn is usually required per time step: increasing this value lead to numerical instability. With these restrictions, the AMI method requires much smaller time steps than the MRF method. Therefore, the MRF method is adopted in this work to employ larger time steps and hence complete simulations in a faster runtime.

For shearing simulations, a large eddy simulation (LES) approach with implicit filtering (i.e. specifying only the filter width) is used to handle turbulence. A one equation eddy-viscosity sub-grid scale model that simulates the behaviour of

Table 1
Composition of A6060 for material properties calculation in VMS.

Element	Al	Si	Mg	Fe	Mn	Cu	Zn	Ti
Composition (mass%)	Balance	0.45	0.475	0.2	0.05	0.05	0.075	0.05

Table 2
Model parameters for MC-DC casting simulation of A6060.

Parameter	Quantity
Casting velocity $\boldsymbol{u}_s$ (m s^{-1})	(0, 0, −0.002917)
Inlet temperature (K)	933
Liquidus temperature T_l (K)	929.250
Solidus temperature T_s (K)	757.375
Solid packing fraction g_c	0.3
Coherency temperature T_c (K)	925.500
Latent heat L_f (J kg^{-1})	375696.0
Density ρ_{ref} (kg m^{-3})	2608.820
Thermal expansion coefficient β_T (K^{-1})	23×10^{-6}
Mushy region momentum sink coefficient K_p (s^{-1})	1.522×10^{7}
Maximum Courant number	0.5

Table 3
Solutal properties for A6060 [41].

Solute	Si	Mg	Fe	Mn	Cu	Zn	Ti
Partition coefficient k_p	0.10	0.32	0.02	0.63	0.13	0.32	0.12
Liquid diffusivity D_l (m^2 s^{-1})	3×10^{-9}	3×10^{-9}	3×10^{-9}	3×10^{-9}	3×10^{-9}	3×10^{-9}	3×10^{-9}
Solution expansion coefficient β	-3.7×10^{-4}	1.3×10^{-4}	-4.6×10^{-3}	-1.0×10^{-3}	-1.2×10^{-3}	-1.3×10^{-3}	-4.5×10^{-4}

Table 4
Composition of AZ31.

Element	Mg	Al	Zn	Mn
Composition (mass%)	Balance	2.92	0.85	0.36

the turbulent kinetic energy [38] is added to resolve the turbulent flow around the rotor-stator region [5]. While Reynolds-Averaged Navier Stokes (RANS) models can predict flow features around the mixer, they severely under-predict the global turbulent energy dissipation rate ε [39]. The discrepancies in predicting turbulent quantities are presumed to originate from Reynolds averaging, with large eddy simulation (LES) kinetic energy predictions being more accurate [40]. The turbulent kinetic equation

$$\frac{\partial(\rho k)}{\partial t} + \nabla \cdot (\rho \boldsymbol{u} k) = \nabla \cdot \left(\rho \nu_{eff} \nabla k\right) + \rho G - \frac{2}{3}\ \rho k \nabla \cdot \boldsymbol{u} - \frac{C_e\ \rho k^{\frac{3}{2}}}{\Delta} \tag{10}$$

is solved, from which the turbulent viscosity is recovered from

$$\mu_t = \rho C_k \Delta k^{\frac{1}{2}}. \tag{11}$$

$G = \nu_t \cdot (\nabla \cdot \boldsymbol{u}) \cdot \mathrm{dev}(2\bar{\boldsymbol{D}})$ where $\nu_t = \mu_t/\rho$ and $\bar{\boldsymbol{D}} = \frac{1}{2}(\nabla \boldsymbol{u} + \nabla \boldsymbol{u}^T)$ is the resolved strain rate tensor. The deviatoric component of tensor $\bar{\boldsymbol{D}}$ is $\mathrm{dev}(\bar{\boldsymbol{D}}) = \bar{\boldsymbol{D}} - \frac{1}{3}(\mathrm{tr}(\bar{\boldsymbol{D}}))\boldsymbol{I}$. $\boldsymbol{I}$ is the identity matrix and tr() denotes the trace operator. $\nu_{eff} = \nu + \nu_t$. $C_e = 1.048$ and $C_k = 0.094$ are model coefficients. The length scale Δ is the cube root of the computational cell volume.

2.3. Material properties and model parameters

The material properties (liquid fraction, specific heat capacity, and density) for A6060 (composition given in Table 1) were calculated using VMS [36] and are plotted in Fig. 3. For specific heat capacity, the values in the transition region were calculated using the method of mixtures using the liquidus and solidus values. Other model parameters are listed in Table 2. Thermal conductivity and viscosity values were estimated from experimental measurements of similar alloys in the literature [14]. The solutal properties, calculated using the ProCAST material database [41], are listed in Table 3. For the magnesium alloy case, the material properties of AZ31 (see composition in Table 4) are taken from the literature [42] and presented in Table 5. The maximum time step used in the simulations is controlled by the specified maximum Courant number.

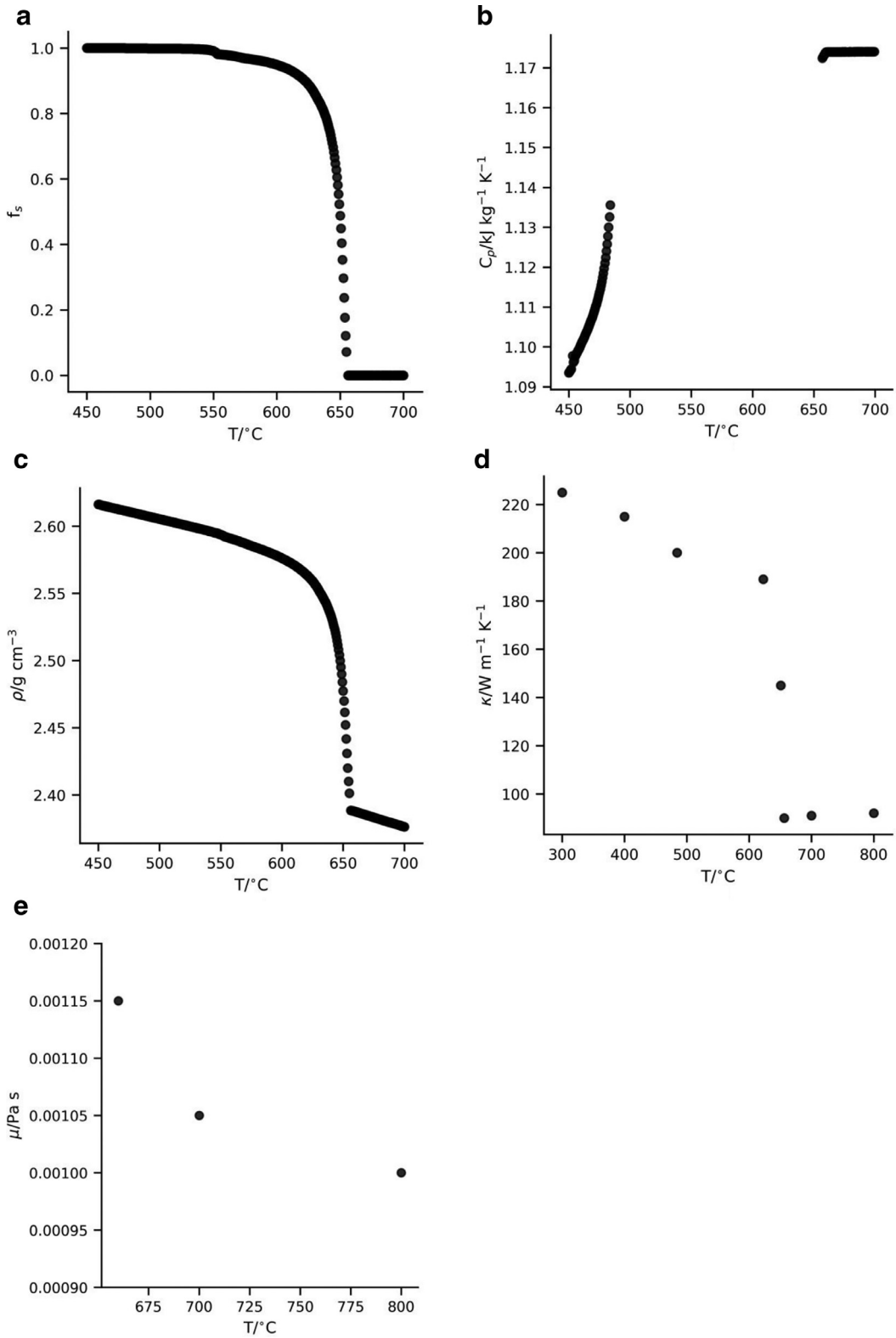

Fig. 3. Variation of material properties of A6060 with temperature as calculated by VMS [36]. Linear interpolation is used for intermediate points, except for specific heat capacity, where $\boldsymbol{c_p}$ between the solidus and liquidus temperatures is interpolated using the solid fraction curve as $\boldsymbol{c_p}(\boldsymbol{T}) = \boldsymbol{c_{p,s}}\boldsymbol{f_s} + \boldsymbol{c_{p,l}}(1 - \boldsymbol{f_s})$ where $\boldsymbol{c_{p,s}}$ and $\boldsymbol{c_{p,l}}$ are, respectively, the specific heat capacities at solidus and liquidus temperatures.

Table 5
Model parameters for MC-DC casting simulation of AZ31 [42].

Parameter	Quantity
Casting velocity $\boldsymbol{u}_s$ (m s^{-1})	(0, 0, −0.004)
Inlet temperature (K)	968.13
Liquidus temperature T_l (K)	903.13
Solidus temperature T_s (K)	848.13
Solid packing fraction g_c [49,50]	0.9
Coherency temperature T_c (K)	897.63
Latent heat L_f (J kg^{-1})	377,000
Specific heat capacity c_p (J kg^{-1} K^{-1})	1050
Density ρ_{ref} (kg m^{-3})	1750
Thermal expansion coefficient β_T (K^{-1})	23×10^{-6}
Thermal conductivity κ (W m^{-1} K^{-1})	80
Dynamic viscosity μ (kg m^{-1} s^{-1})	$0.001 \cdot \exp[-13.82 \cdot (T-T_l)/(T_l-T_s)]$ 0.001 when $T > T_l$
Mushy region momentum sink coefficient K_p (s^{-1})	1.522×10^7
Maximum Courant number	0.5

3. Numerical implementation

The present finite volume code is based on the solver *buoyantPimpleFoam* of the open source library OpenFOAM version 5.x (OF5.x) [43]. The following changes were made to the original source code of OF5.x:

3.1. Secondary cooling heat transfer boundary condition

The heat transfer coefficient at the mould is estimated from measurements in a DC casting experiment and entered as a table at the wall. The tabular boundary condition is implemented by modifying the *compressible: externalWallHeatFluxTemperatureFvPatchScalarField* class [43] to read an interpolation table.

The forced-convection heat transfer coefficient is evaluated using the following non-dimensional formula [19]

$$h_{conv} = 0.01\,\mathrm{Pr}^{\frac{1}{3}}\left(\frac{4\Gamma}{\mu}\right)^{\frac{1}{3}}\left(\frac{\mu^2}{k^3{\rho_l}^2 g}\right)^{\frac{1}{3}}. \tag{12}$$

The Rohsenhow formula [44] is used to consider the effect of nucleate boiling

$$q''_{boil} = h_{boil}(T - T_{water}) = \mu L_v\sqrt{\frac{g(\rho_l - \rho_v)}{\sigma}}\left(\frac{C_p \Delta T}{L_v \mathrm{Pr} C_{sf}}\right), \tag{13}$$

where $\Delta T = T - T_{sat}$ is the difference between the local surface temperature and the water saturation temperature T_{sat} and $\mathrm{Pr} = c_p\mu/\kappa$ is the Prandtl number. The heat transfer coefficient then is evaluated as

$$h_q = \begin{cases} h_{conv} & \text{if } q''_{incp} \le q''_{conv} \\ h_{conv} + h_{boil} & \text{if } q''_{incp} > q''_{conv} \end{cases}, \tag{14}$$

where the heat transfer at incipient boiling is given by

$$q''_{incp} = 3910\ \Delta T^{2.16} \tag{15}$$

and $q''_{conv} = h_{conv}(T - T_{water})$. Table 6 lists the material properties used for water. The values for h_{boil} are computed using Eq. (13) using a Python script for the range of temperatures covered by the simulation. The values of h_q are then computed and used in the table interpolation method.

Table 6
Water properties at saturation temperature [19].

Property	Quantity
Saturation temperature T_{sat} (K)	372.8
Water film temperature T_{water} (K)	293.13
Liquid density ρ_l (kg m^{-3})	958.6
Vapor density ρ_v (kg m^{-3})	0.5903
Latent heat of vaporization L_v (J kg^{-1})	2257000.0
Thermal conductivity κ (W m^{-1} K^{-1})	0.6790
Specific heat capacity c_p (J kg^{-1} K^{-1})	4215
Surface tension σ (N m^{-1})	0.059
Flow rate per unit circumference Γ (m^2 s^{-1})	0.00308
Nucleate boiling constant C_{sf}	0.011

The wall temperature is under-relaxed for numerical stability, i.e. the temperatures in cells adjacent to the water-cooled walls are updated at the next loop $n+1$ using $T^{n+1} = T^n + \Omega(T^{n+1} - T^n)$. Upon convergence of the linearized heat transfer equation, the difference between T^{n+1} and T^n become zero, thereby having no effect on energy balance. Stability was achieved using an under-relaxation coefficient $\Omega = 0.9$.

3.2. Tabular material properties

The material properties in Fig. 3 are implemented as a new *fluidThermo* model in OpenFOAM that reads temperature dependent properties from a table and linearly interpolates them in each computational cell.

3.3. Mushy zone melting solidification source terms

The *fv::meltingSolidificationSource* class is modified to include a liquidus and solidus temperature. The liquid fraction is obtained iteratively using the procedure described in [45]. Eq. (3) is solved for h^{k+1} with f_l^k

$$\frac{\partial\left(\rho h^{k+1}\right)}{\partial t} + \nabla\cdot\left\{\rho(\boldsymbol{u}-\boldsymbol{u}_m)h^{k+1}\right\} = \nabla\cdot\left(\kappa\nabla T^{k+1}\right) - L_f\left[\frac{\partial\left(\rho f_l^k\right)}{\partial t} + \nabla\cdot\left\{\rho(\boldsymbol{u}-\boldsymbol{u}_m)f_l^k\right\}\right] \tag{16}$$

The phase fraction is then updated as

$$f_l^{k+1} = f_l^k + \Omega\frac{C_p}{L_f}\left(T^{k+1} - T^*\right) \tag{17}$$

where T^* is interpolated from a lookup table of temperature against liquid fraction in the solidus-liquidus range. An under-relaxation factor $\Omega \sim 0.1$ is required for numerical stability. For boundedness, the liquid fraction is forced to be between 0 and 1.

$$f_l^{k+1} = \min\left(\max\left(f_l^{k+1}, 0\right), 1\right) \tag{18}$$

Since material properties are liquid fraction dependent, the material properties are updated within each loop. The iterative procedure is iterated over at least 3 times until residuals of enthalpy and melt liquid fraction are below a desirable tolerance of 1×10^{-8}).

3.4. Discretization schemes and solver control parameters

Table 7.

3.5. Boundary conditions

Fig. 4 and Table 8 show the boundary conditions for the simulations. Radiative heat loss is ignored.

Table 7
Discretization schemes and solver control parameters. The default scheme entry corresponds to the scheme that is used for the relevant terms that are not explicitly mentioned in the table.

Discretization schemes	
Transient term discretization ($\partial/\partial t$)	Euler
Default gradient scheme (∇)	Gaussian integration with linear interpolation
∇U, ∇k, $\nabla\omega$	Bounded Gaussian integration with linear interpolation
Default divergence scheme ($\nabla\cdot$)	Bounded Gaussian integration with linear interpolation
$\nabla\cdot\phi\boldsymbol{R}$, $\nabla\cdot\phi K$, $\nabla\cdot\phi E_{kp}$, $\nabla\cdot\boldsymbol{R}$, $\nabla\cdot\phi_m p$, $\nabla\cdot\{\rho\nu_{eff}[(\nabla\boldsymbol{U})^T - \frac{1}{3}tr[(\nabla\boldsymbol{U})^T]\boldsymbol{I}]\}$	Gaussian integration with linear interpolation
Laplacian scheme ($\nabla\cdot(\Gamma\nabla)$)	Gaussian integration with linear interpolation and explicit non-orthogonal correction
Interpolation scheme	Linear interpolation
Surface normal gradient scheme	Explicit non-orthogonal correction
Solver control parameters	
ρ, p, T	Preconditioned conjugate gradient (PCG) with simplified diagonal-based incomplete Cholesky (DIC) preconditioner
$\boldsymbol{U}$, h, k, ω, $\boldsymbol{R}$	Preconditioned bi-conjugate gradient (PBiCG) with simplified diagonal-based incomplete LU (DILU) preconditioner
Momentum predictor	Yes
Number of outer correctors loops	1
Number of inner correctors loops	2
Number of energy correctors loops	3
Number of non-orthogonal correctors loops	0

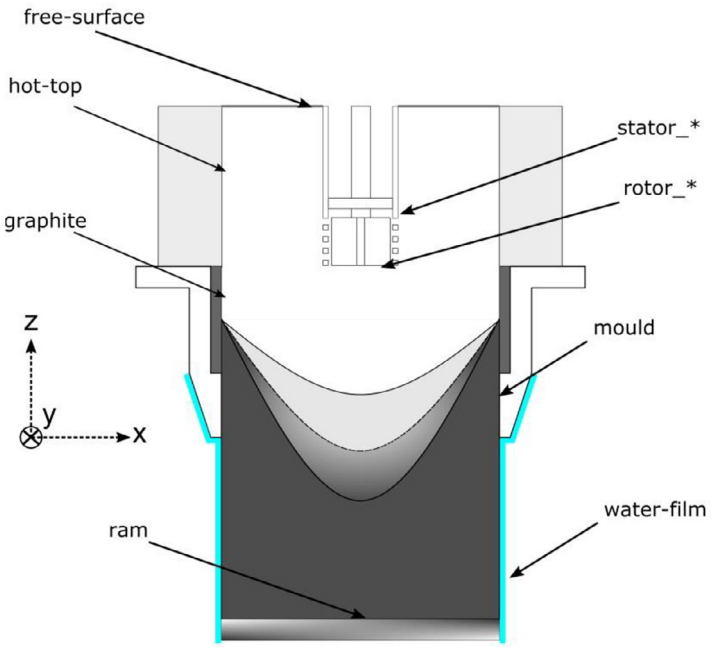

Fig. 4. Boundary conditions for MC-DC simulations.

Table 8
Boundary conditions for MC-DC simulations. The boundary names are as labelled in Fig. 4.

U	
ram	Dirichlet boundary condition with a fixed value of (0, 0, −0.002917) m s^{-1}
water-film|mould|graphite|ceramic|hot-top|rotor_stop|stator_patch.*	No slip boundary condition $\boldsymbol{U} = 0$
rotor_*	Moving wall velocity set to **0** relative to rotating frame
free-surface	Neumann boundary condition, i.e. zero normal gradient
p	
ram	Fixed flux pressure, value 1×10^5 Pa
free-surface	Dirichlet boundary condition with a fixed value of 1×10^5 Pa
water-film|mould|graphite|ceramic|hot-top|stator_patch.*|rotor_.*|.*	Fixed flux pressure, value 1×10^5 Pa
T	
ram	Inlet-outlet, internal value when inflow, Neumann boundary condition, i.e. zero normal gradient when outflow
free-surface	Dirichlet boundary condition with a fixed value of 933 K
hot-top|stator_patch.*|rotor_.*	Adiabatic or Neumann boundary condition, i.e. zero normal gradient
water-film|mould|graphite|ceramic	Heat transfer coefficient prescribed from a lookup table, values calculated from [44] External temperature set to 293.0 K
k	
ram	Neumann boundary condition, i.e. zero normal gradient
free-surface	Dirichlet boundary condition with a fixed value of 5.58×10^{-8} m^2 s^{-2}
water-film|mould|graphite|ceramic|hot-top|stator_patch.*|rotor_.*	class *kqRWallFunction*, equivalent to a Neumann boundary condition, i.e. zero normal gradient
ω	
ram	Neumann boundary condition, i.e. zero normal gradient
free-surface	Dirichlet boundary condition with a fixed value of 0.001 s^{-1}
water-film|mould|graphite|ceramic|hot-top|stator_patch.*|rotor_.*	class *omegaWallFunction*, wall function computed from [51]

4. Results and discussion

4.1. DC casting of A6060

To validate the numerical model, a DC casting setup was simulated in a two-dimensional axisymmetric model without the rotor-stator mixer to compare with measured temperature profiles along the axis and sidewall of the caster. Fig. 5 shows the comparison between the predicted and measured temperature profiles. The measured temperatures are shown

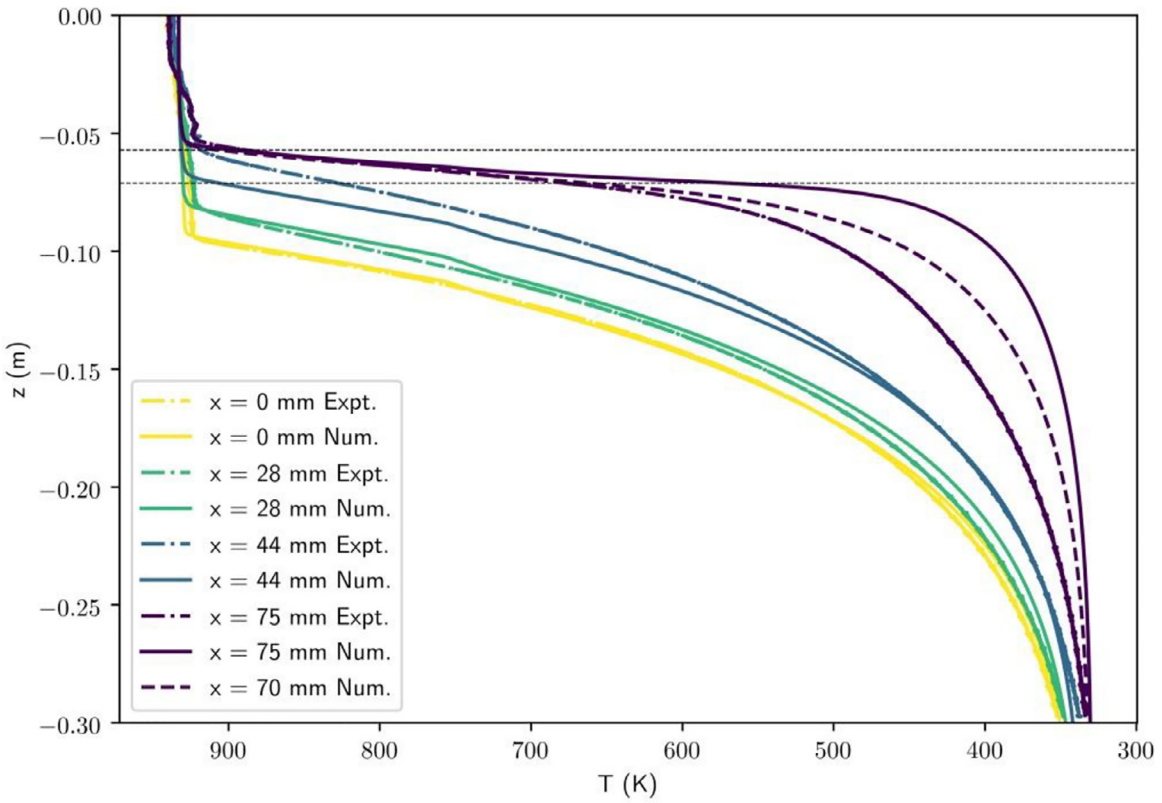

Fig. 5. Comparison between predicted temperatures (solid line or dashed line in position corresponding to the surface of the billet) and measurements (line dot). The two horizontal lines represent the (aluminium) mould position. The ***x*** axis is as indicated in Fig. 1.

with dash-dotted lines. At all measured positions, the temperature decreases in the melt because of heat conduction towards the secondary cooling walls. The near surface measurement (labelled '$x = 75$ mm') demonstrates a large heat extraction rate near the walls, resulting in faster solidification. Note that the comparison with experiment is poorer than at the other radial positions due to a larger uncertainty in the position of the thermocouple and the difficulty in obtaining the exact boundary conditions due to cooling. However, this error decreases for measurements nearer to the billet centre. A mesh refinement study was performed to examine the spatial convergence of the simulation. The result of this analysis is summarized in Fig. 6 and the mesh with 20,736 cells can be deemed to yield a grid-independent solution. This corresponds to an average cell length of ∼1 mm.

Since the packing fraction g_c is assumed to be 0.3, using a similar value to that encountered in the literature [13,46], a sensitivity analysis is run with the packing fraction assuming to range from 0.3 to 0.6. Fig. 7 shows the results of this analysis and the assumed value of 0.3 yields the closest comparison with measured temperatures. This packing fraction is therefore used for simulations of MC-DC casting of A6060.

Fig. 8 shows a slice of the sump profile along the axis of the billet. The results are consistent with profiles reported in the literature, e.g. [13,47]. The coherency isosurface, i.e. the temperature at the packing fraction $g_c = 0.3$, is almost paraboloid – represented by the black dashed line in the plotted slice –, with velocities decreasing in value nearer to the mushy region. Convection results in a flatter liquidus line above the sump [47]. The corresponding temperature gradients and cooling rates are shown in Fig. 9. The heat transfer is larger near the boundary as expected. The large values of temperature gradient at the boundaries imply that columnar growth will occur from the billet walls. The cooling rate is low throughout the domain, with slightly elevated values at the solidification front where the temperature gradients are high and flow velocities still appreciable.

4.2. MC-DC casting of A6060

In this section, the numerical results for shearing A6060 at 4000 RPM using the mixer depicted in Fig. 2 are presented. All computations of MC-DC were performed in three-dimensions. To resolve the fluid flow in the mixer region accurately, each stator hole has 24 cells along the hole section and the rotor-stator gap is resolved with 8 cells, i.e. with 4 cells on each side of the baffle delimiting the rotating and fixed zones.

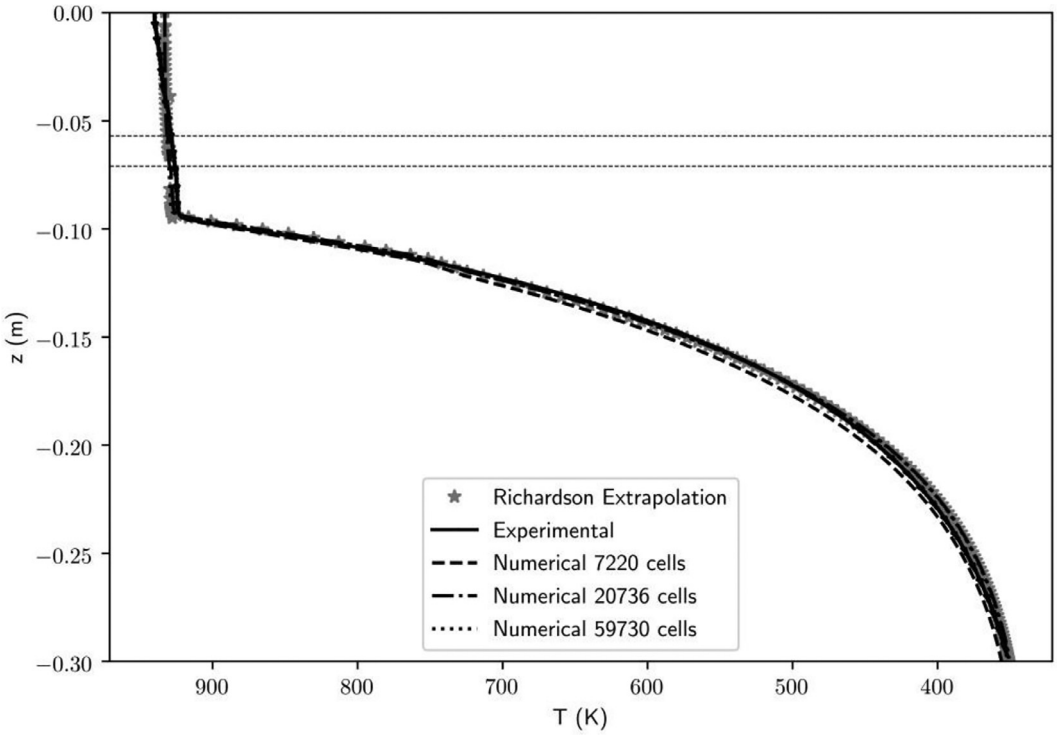

Fig. 6. Grid convergence analysis for the DC casting model. Richardson extrapolation of the temperature at the centre ($\boldsymbol{x} = 0$ mm) reveals that a mesh with 20,736 cells is suitable for modelling the heat transfer in the billet.

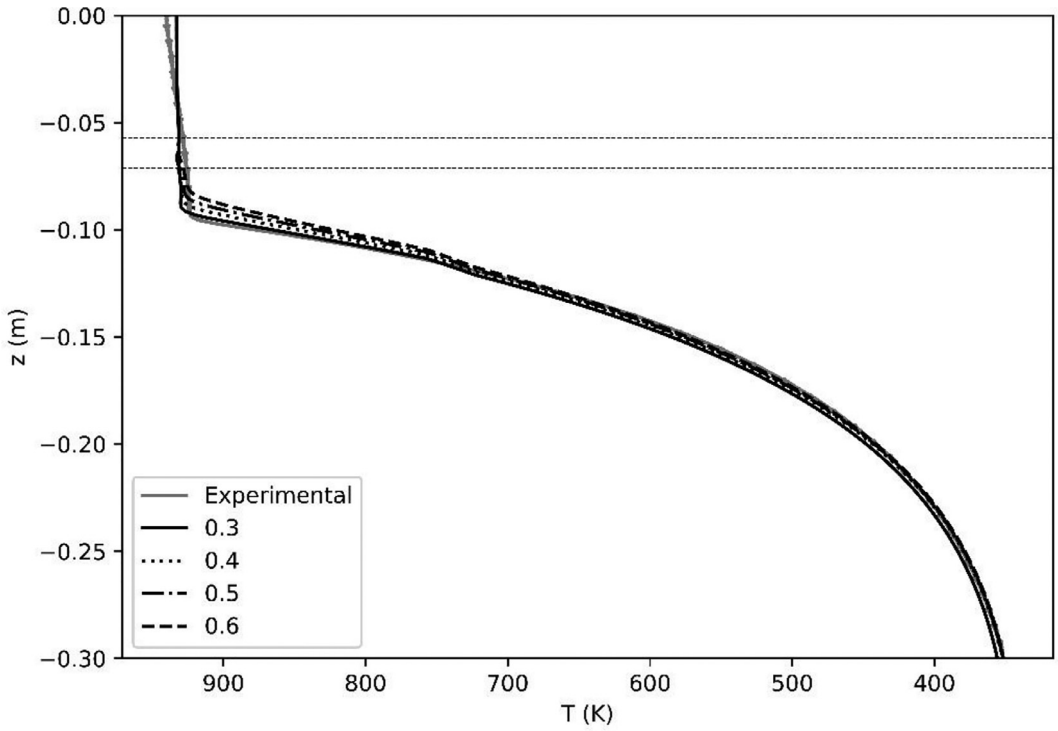

Fig. 7. Influence of packing fraction $\boldsymbol{g_c}$ on the predicted temperature at the centre ($\boldsymbol{x} = 0$ mm). The prediction assuming $\boldsymbol{g_c} = 0.3$ yields the closest match with measured temperatures (in gray).

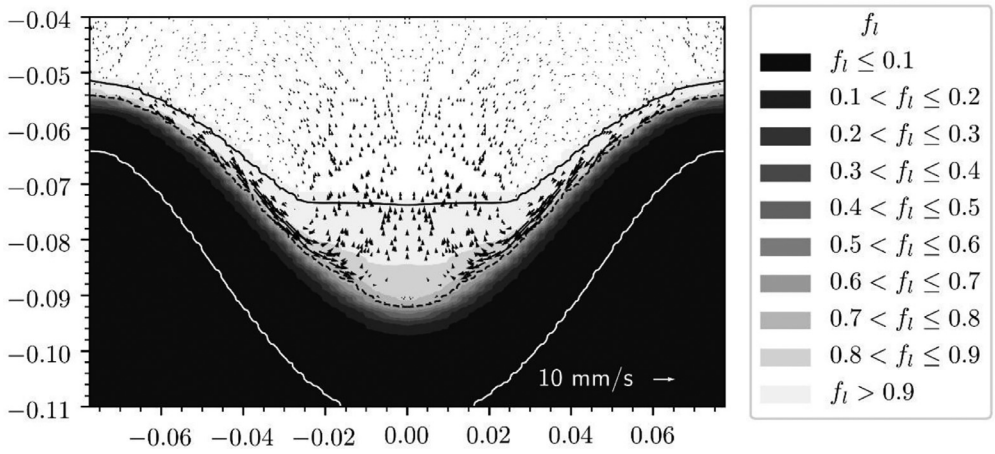

Fig. 8. Contour map of liquid fraction f_l and velocity field across the axis of the DC caster along the slice $y = 0$ mm. The black solid line represents the liquidus temperature. The black dashed line represents the coherency temperature. The while solid line represents the solidus temperature.

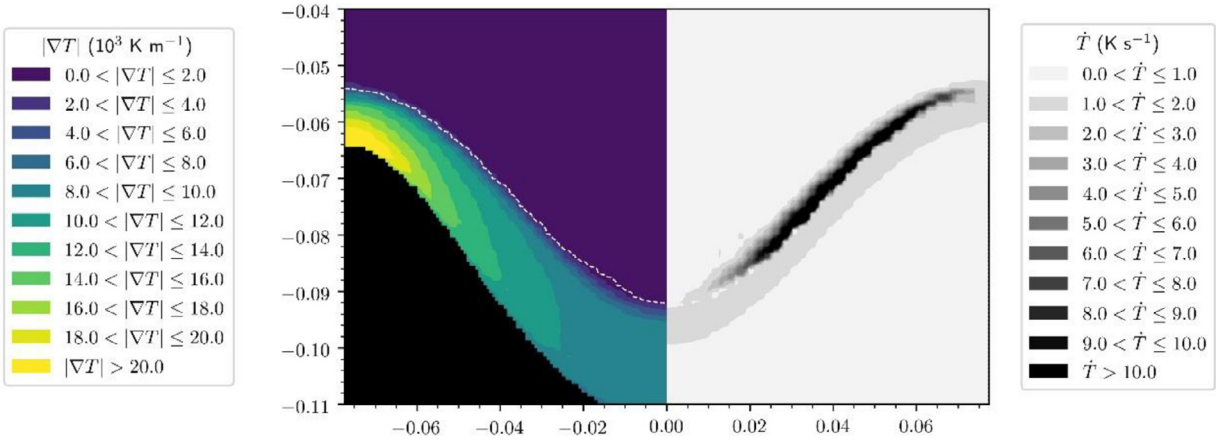

Fig. 9. Contour map of temperature gradient magnitude ∇T (left) and cooling rate $\dot{T}$ (right) across the axis of the DC caster along the slice $y = 0$ mm. The temperature gradient contour map is plotted above the solidus temperature and the cooling rate contour map is plotted between the solidus and liquidus temperatures. The white dashed line represents the coherency temperature.

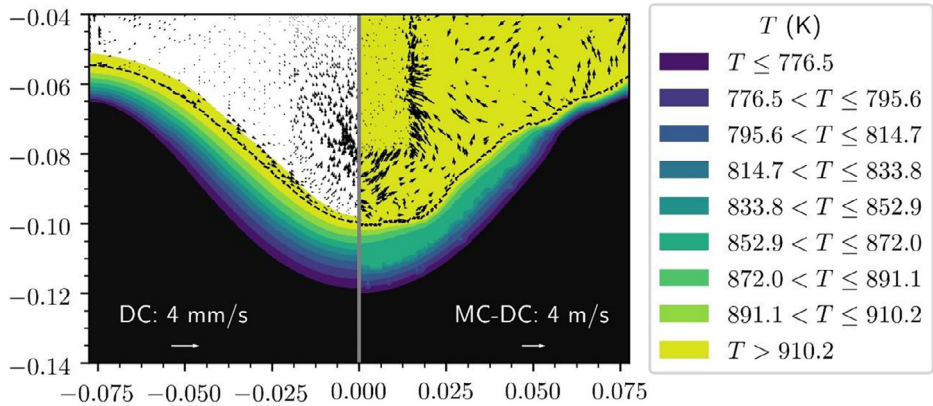

Fig. 10. Comparison of sump profile between conventional DC casting (left) and MC-DC casting (right) of A6060 in a 155 mm mould along the slice $y = 0$ mm. The temperature range of contours is the liquidus to solidus range of A6060. The velocity fields across the axis of the billets have different scales. The dotted line denotes the coherency temperature.

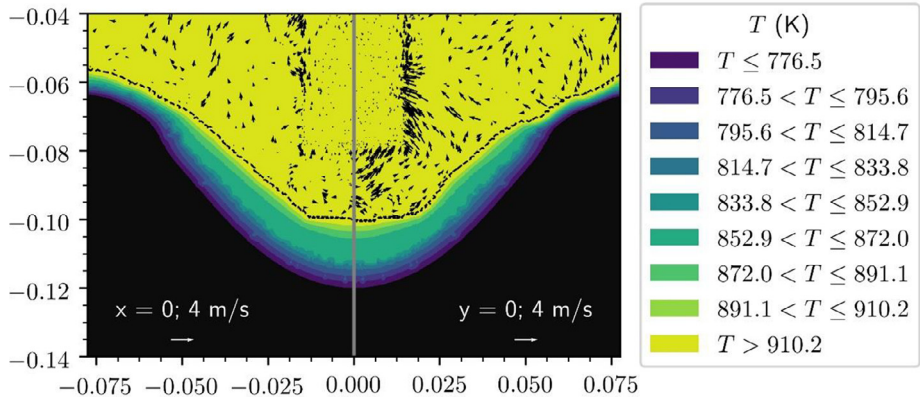

Fig. 11. Comparison of sump profiles in the MC-DC casting of A6060 in a 155 mm mould along the slices $\boldsymbol{x} = 0$ mm and $\boldsymbol{y} = 0$ mm. The temperature range of contours is the liquidus to solidus range of A6060. The dotted line denotes the coherency temperature.

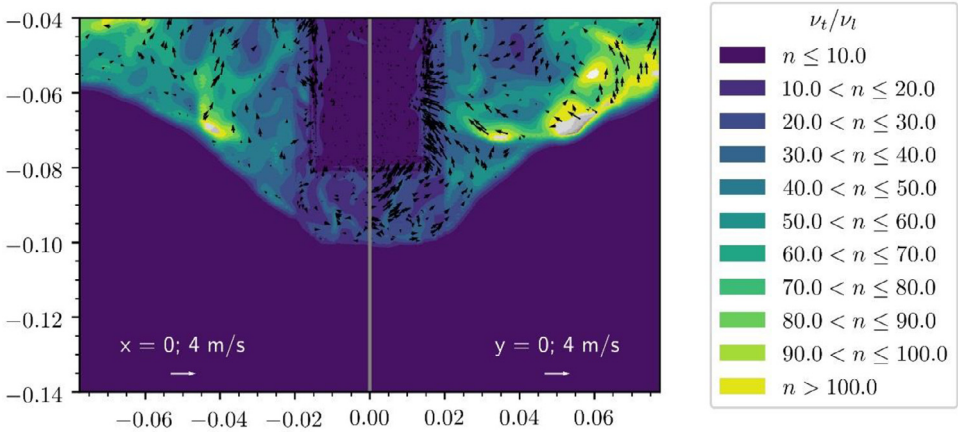

Fig. 12. Comparison of turbulent viscosities in the MC-DC casting of A6060 in a 155 mm molud along the slices $\boldsymbol{x} = 0$ mm and $\boldsymbol{y} = 0$ mm. The turbulent viscosities are normalized by laminar viscosity.

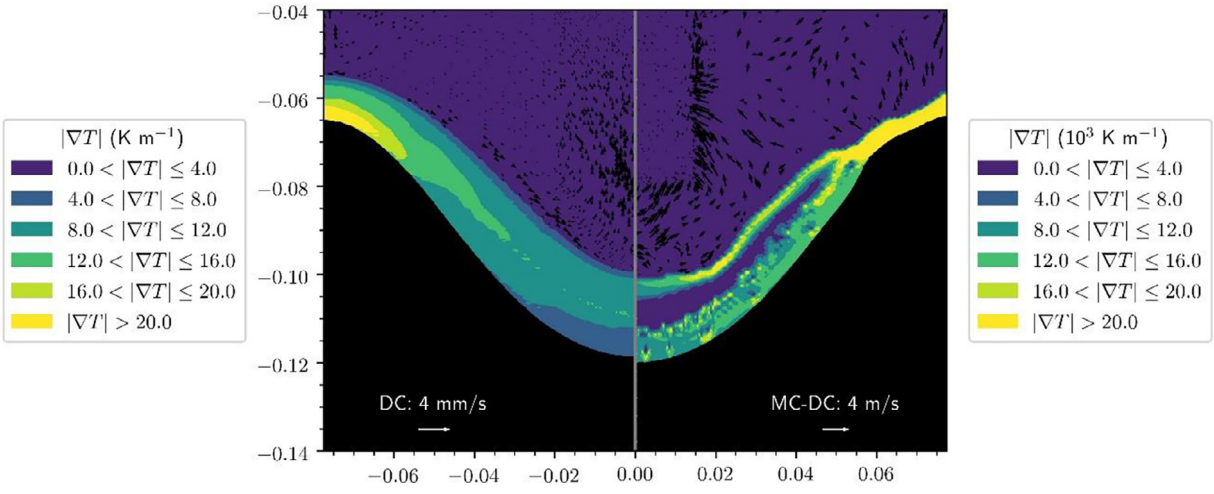

Fig. 13. Comparison of temperature gradients between conventional DC casting (left) and MC-DC casting (right) of A6060 in a 155 mm mould along the slice $\boldsymbol{y} = 0$ mm. The velocity fields across the axis of the billets have different scales.

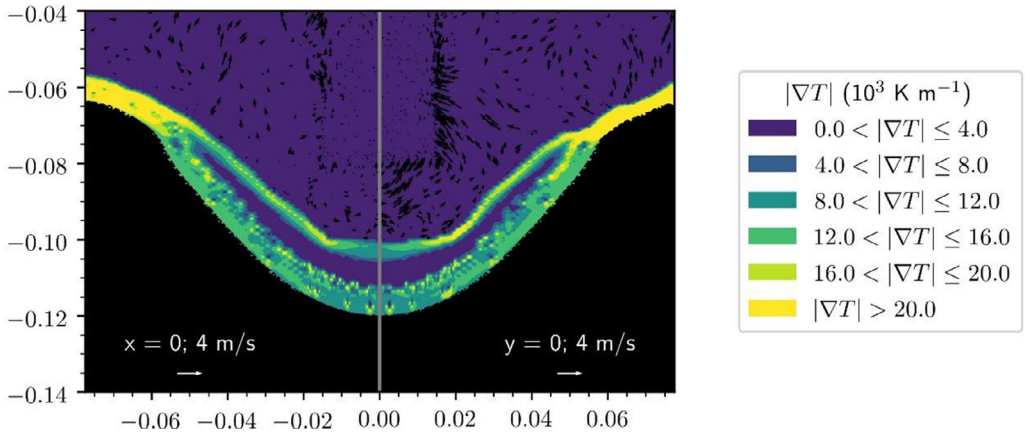

Fig. 14. Comparison of temperature gradients in the MC-DC casting of A6060 in a 155 mm mould along the slices $\boldsymbol{x} = 0$ mm and $\boldsymbol{y} = 0$ mm.

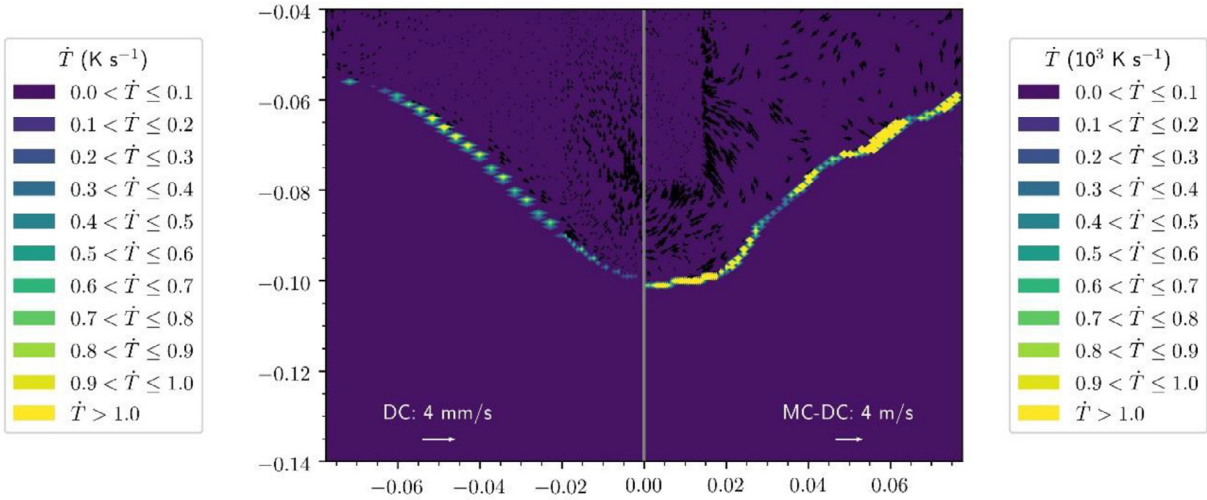

Fig. 15. Comparison of cooling rates between conventional DC casting (left) and MC-DC casting (right) of A6060 in a 155 mm mould along the slice $\boldsymbol{y} = 0$ mm. The velocity fields across the axis of the billets have different scales. The cooling rates for MC-DC are 3 orders of magnitudes larger than in conventional DC casting.

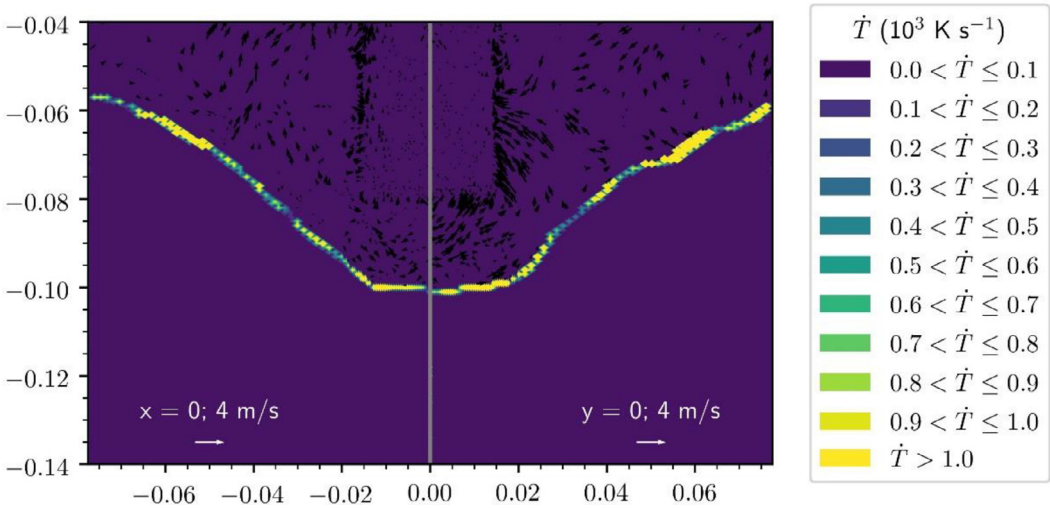

Fig. 16. Comparison of cooling rates in the MC-DC casting of A6060 in a 155 mm mould along the slices $\boldsymbol{x} = 0$ mm and $\boldsymbol{y} = 0$ mm.

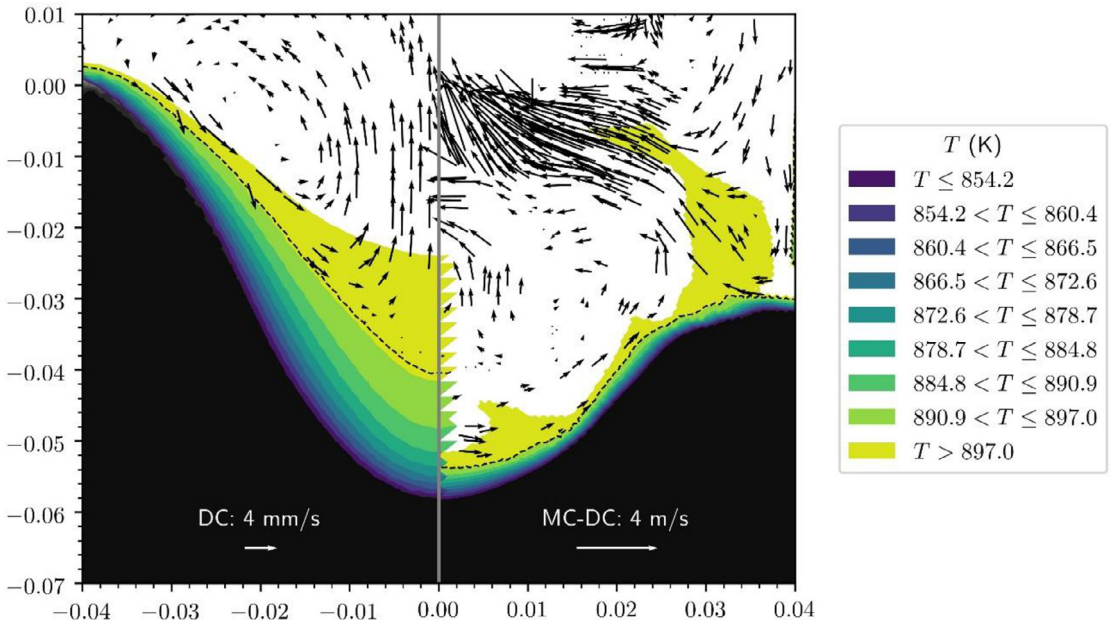

Fig. 17. Comparison of sump profile between conventional DC casting (left) and MC-DC casting (right) of AZ31 in an 80 mm mould along the slice $\boldsymbol{y} = 0$ mm. The temperature range of contours is the liquidus to solidus range of AZ31. The velocity fields (minus the casting speed) across the axis of the billets have different scales. The dotted line denotes the coherency temperature.

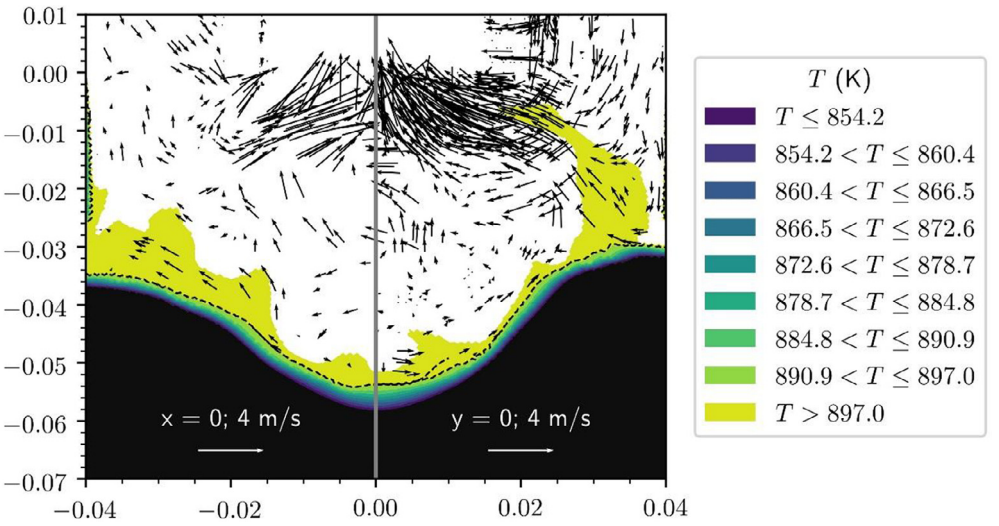

Fig. 18. Comparison of sump profiles in the MC-DC casting of AZ31 in an 80 mm mould along the slices $\boldsymbol{x} = 0$ mm and $\boldsymbol{y} = 0$ mm. The temperature range of contours is the liquidus to solidus range of AZ31. The dotted line denotes the coherency temperature.

Fig. 10 shows a comparison of the sump profile between conventional DC casting (labelled DC) and melt-conditioned direct-chill casting (labelled MC-DC) along the slice $y = 0$ mm. The jets from the mixer result in a large convectional flow from the mould walls towards the centre of the billet. This flow entrains slurry towards the centre of the billet and harmonizes the temperature field in the liquid pool to the liquidus temperature. The solution is quasi-axisymmetric as shown in Fig. 11: the sump profile is similar along both $x = 0$ mm and $y = 0$ mm slices. The flow is turbulent in the sump, as shown by the large turbulent viscosities around the mixer in Fig. 12.

The results presented in the figures are a snapshot in time of the sump profile after the coherency isosurface has stopped moving, thus indicating that a quasi-steady state solution is achieved. While the coherency isosurface is stable, the flow in the slurry and liquid regions are turbulent and vary chaotically. However, the conclusions of the research are not affected since the sump profile and temperature gradients are of interest in this study.

The increased convection rate results in a larger temperature gradient at the solidification front, as shown in Fig. 13. The cooling rate in the sump, shown in Fig. 15, is larger inside the modified sump due to the large speed motion of the slurry

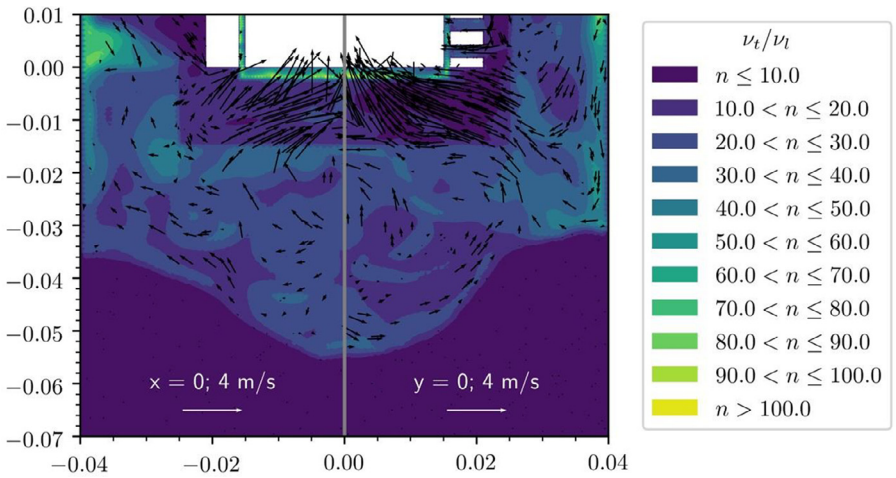

Fig. 19. Comparison of turbulent viscosities in the MC-DC casting of AZ31 in an 80 mm mould along the slices $\boldsymbol{x} = 0$ mm and $\boldsymbol{y} = 0$ mm. The turbulent viscosities are normalized by laminar viscosity.

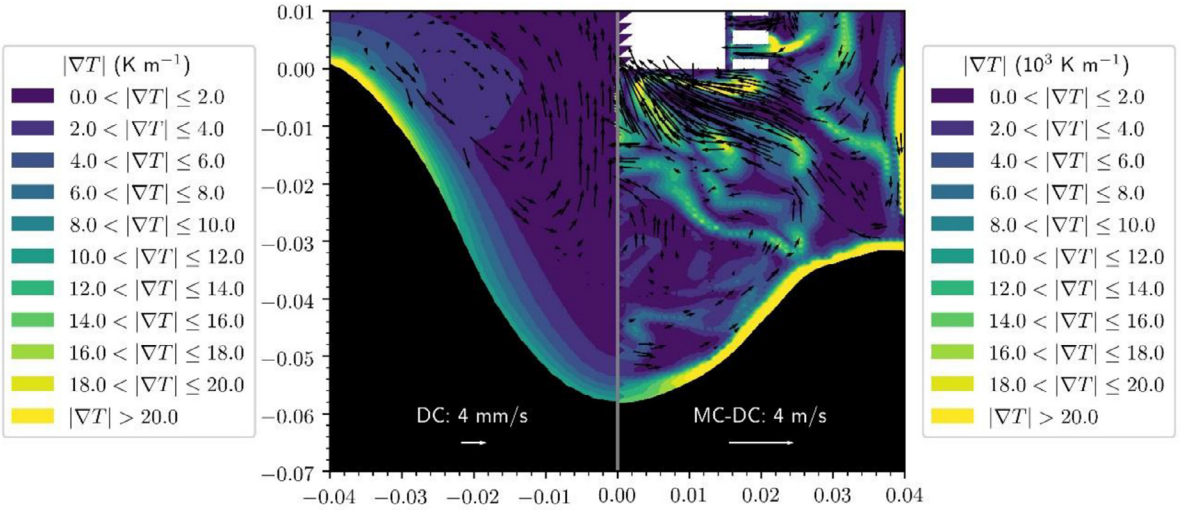

Fig. 20. Comparison of temperature gradients between conventional DC casting (left) and MC-DC casting (right) of AZ31 in an 80 mm mould along the slice $\boldsymbol{y} = 0$ mm. The velocity fields across the axis of the billets have different scales.

and floating dendrites, resulting in transient changes in the local temperature. The larger cooling rate values of the order of 10^3 K s^{-1} indicate that smaller dendrite arm spacings ~5 μm are expected with melt shearing [48]. Figs. 14 and 16 also show that the solution is quasi-axisymmetric, with no significant differences between solutions in two perpendicular planes. The large speed of the rotor and the cylindrical symmetry of the stator both contribute to a solution that is independent of the azimuthal direction.

4.3. MC-DC casting of AZ31

This section presents the results upon shearing AZ31 in an 80 mm diameter mould, similar to a previous experiment [31], at 4000 RPM. All the MC-DC computations are in three-dimensions. In this simulation, an air gap is modelled in the primary cooling region (aluminium mould). The air gap thickness is estimated at 3 mm in the bottom half of the mould, with the thermal conductivity of air assumed to be 0.060 W m^{-1} K^{-1}. Fig. 17 shows the comparison between the sump profiles in conventional DC casting and MC-DC casting. In conventional DC casting (Fig. 17 left), the liquidus line is not flat due to the fast pulling speed of 4 mm/s. The vectors represent velocities in the frame of the sump, i.e. with the casting speed subtracted. The flow rate is negligible in the mushy zone (below the coherency temperature). There is only one large recirculation when looking at the axis: due to natural convection, the melt flows upwards that the centre of the billet, leading to the large vortex with flow going downwards to the sides due to continuity. Fig. 18 show that the results are

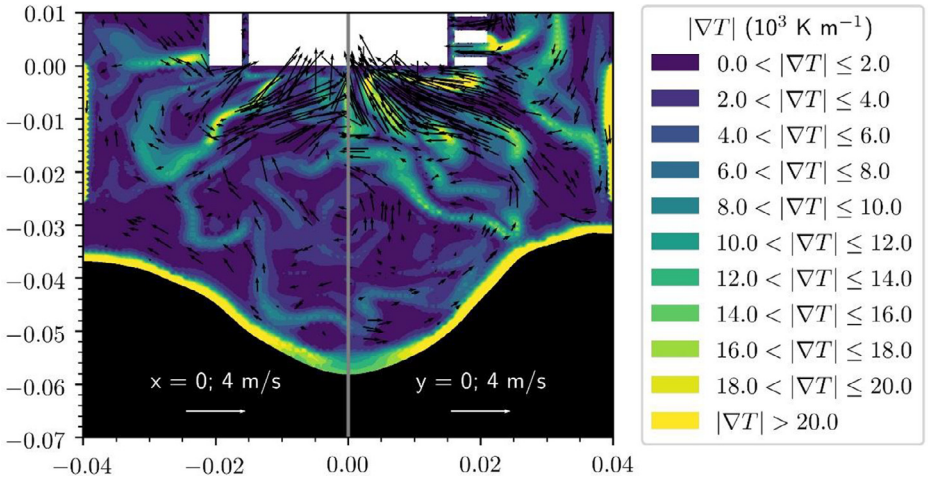

Fig. 21. Comparison of temperature gradients in the MC-DC casting of AZ31 in an 80 mm mould along the slices $\boldsymbol{x} = 0$ mm and $\boldsymbol{y} = 0$ mm.

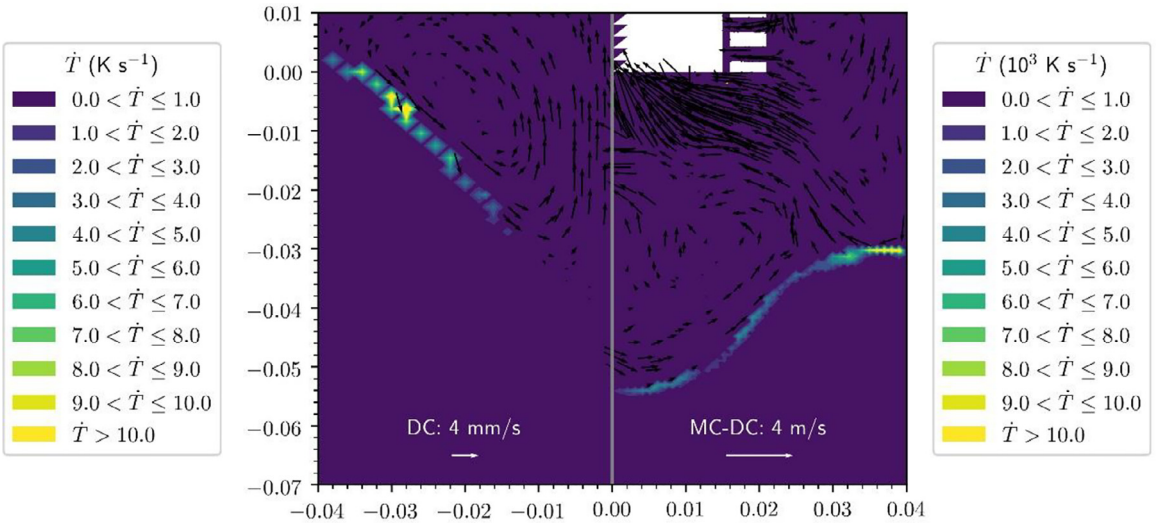

Fig. 22. Comparison of cooling rates between conventional DC casting (left) and MC-DC casting (right) of AZ31 in an 80 mm mould along the slice $\boldsymbol{y} = 0$ mm. The velocity fields across the axis of the billets have different scales. The cooling rates for MC-DC are 3 orders of magnitudes larger than in conventional DC casting.

quasi-axisymmetric, with the sump depth similar when measured along perpendicular slices. The flow is turbulent around the mixer as shown in Fig. 19.

Upon shearing after starting from the steady state condition achieved with conventional DC casting (Fig. 17 left), the flow rate is considerably faster (of the order of 1000 times higher) and more turbulent, as demonstrated by the large number of vortices and seemingly chaotic velocity distribution (Fig. 17 right). The sump is shallower than in conventional DC casting. The mixer increases the heat extraction rate in the sump due to the large number of vortices which increase the mixing inside the melt. This is analogous to increasing the thermal conductivity of the melt above the solidification front. The melt that is ejected from the top rows of the stator holes at the liquidus impinges on the mould walls below, thereby preventing solidification upon contact with the mould. Solidification occurs at a lower position, below the pseudo-cavern around the mixer (at around −3 mm). This occurs due to the proximity of the mixer with the mushy zone.

Fig. 20 shows the comparison of temperature gradients inside the sump. The large temperature gradient zone near the solidification front occurs over a larger surface (perpendicular to the plane of the paper), as a result of a shorted distance between the shell formation and the position of the chill (water contact). The temperature gradient in the sump is also chaotic due to the chaotic redistribution of the slurry as it is entrained by the large melt flow. This transient pattern of temperature gradient reflects the chaotic mixing of the melt below the mixer due to turbulence. This results in larger cooling rate values throughout the sump, as shown in Fig. 22 (right). These large cooling rate values promote a finer grain structure in the resulting billet [29]. Figs. 21 and 23 also demonstrate that the temperature gradients and cooling rates are quasi-axisymmetric.

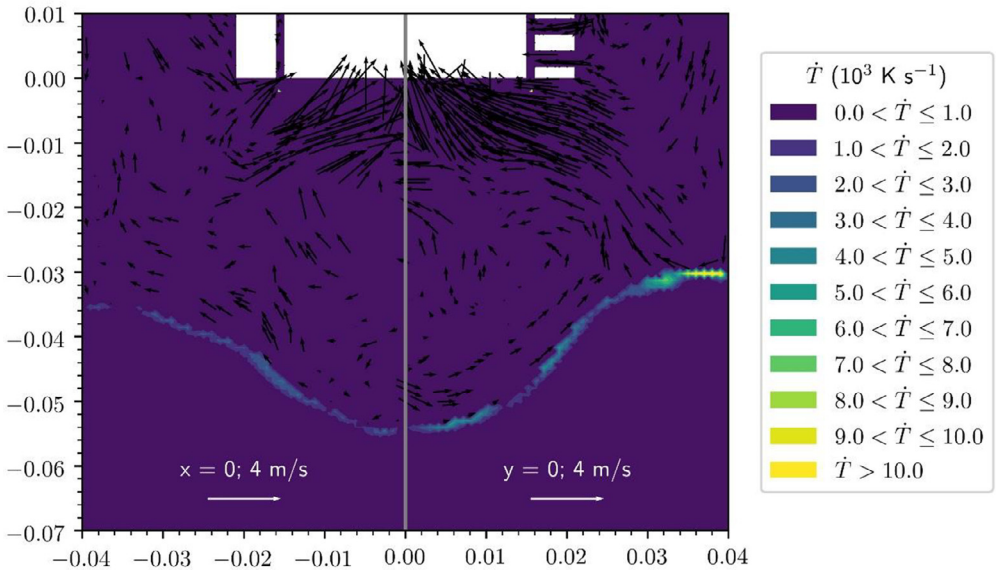

Fig. 23. Comparison of cooling rates in the MC-DC casting of AZ31 in an 80 mm mould along the slices $\boldsymbol{x} = 0$ mm and $\boldsymbol{y} = 0$ mm.

5. Conclusions

The high-shear processing of direct-chill casting has been modelled for the first time and this work presents results of the model for two alloys: A6060 and AZ31. The model is numerically stable and in qualitative agreement with previous results from the literature. In summary:

1. The model is computationally tractable and can be applied to design of experiment studies to optimize the melt-conditioned direct-chill casting process.
2. The flow model is reasonably accurate, with the large eddy simulation model accurately resolving the large vortices inside the sump, thereby resulting in accurate temperature predictions in the sump.
3. Shearing modifies the sump profile by entraining the slurry into the mixer along the axis of the cast billet. The turbulent flow pattern in the melt is chaotic and entrains floating grains towards the melt. The increased heat extraction rate results in a larger temperature gradient at the solidification front.
4. The mixer position significantly modifies the sump depth and position. A mixer immersed near the solidification front results in a shallower sump, with the shell at the mould forming below the pseudo-cavern around the mixer.
5. Larger cooling rates (by 3 orders of magnitudes) are predicted with melt shearing, resulting in a finer grain structure in the billet.

Acknowledgements

Financial support from EPSRC (UK) under grant number EP/N007638/1 is gratefully acknowledged. The authors are thankful for the materials properties provided by Dr Peter Quested and Prof. Alan Dinsdale.

Data availability

The processed data required to reproduce these findings cannot be shared at this time due to technical limitations (their large size ∼TB) and are available upon reasonable request.

Appendix A. OpenFOAM settings

Tables A and B.

Table A
OpenFOAM discretization schemes and solver control parameters.

Discretization schemes	
ddtSchemes	Euler
gradSchemes	
default	Gauss linear
grad(U), grad(k), grad(omega)	cellLimited Gauss linear 1
divSchemes	
default	Bounded Gauss limitedLinear 1
div(phi, R), div(phi, K), div(phi, Ekp), div(R), div(meshPhi,p), div(((rho*nuEff)*dev2(T(grad(U)))))	Gauss linear
laplacianSchemes	
default	Gauss linear corrected
interpolationSchemes	
default	linear
snGradSchemes	
default	corrected
Solver control parameters	
rho, pcorr, p_rgh, T	PCG, DIC
U, h, k, omega, R	PBiCG, DILU
momentumPredictor	Yes
nOuterCorrectors	1
nCorrectors	2
nEnergyCorrectors	3
nNonOrthogonalCorrectors	0

Table B
OpenFOAM boundary condition settings.

U	
ram	Fixed value (0, 0, −0.002917) m s^{-1}
water-film|mould|graphite|ceramic|hot-top|rotor_stop|stator_patch.*	No slip
rotor_*	Moving wall velocity, **0** relative to rotating frame
free-surface	Normal gradient = 0
p	
ram	Fixed flux pressure, value 1×10^5 Pa
free-surface	Fixed value 1×10^5 Pa
water-film|mould|graphite|ceramic|hot-top|stator_patch.*|rotor_.*|.*	Fixed flux pressure, value 1×10^5 Pa
T	
ram	Inlet-Outlet, internal value when inflow, normal gradient = 0 when outflow
free-surface	Fixed value, 933 K
hot-top|stator_patch.*|rotor_.*	Normal gradient = 0 (adiabatic)
water-film|mould|graphite|ceramic	Heat transfer coefficient prescribed from a lookup table, values calculated from [44] External temperature = 293.0 K
k	
ram	Normal gradient = 0
free-surface	Fixed value 5.58×10^{-8} m^2 s^{-2}
water-film|mould|graphite|ceramic|hot-top|stator_patch.*|rotor_.*	class *kqRWallFunction*, Normal gradient = 0
ω	
ram	Normal gradient = 0
free-surface	Fixed value 0.001 s^{-1}
water-film|mould|graphite|ceramic|hot-top|stator_patch.*|rotor_.*	class *omegaWallFunction*, computed from [51]

References

[1] J.H. Grandfield, D.G. Eskin, I.F. Bainbridge, Direct-Chill Casting of Light Alloys, Science and Technology, John Wiley & Sons, Hoboken, NJ, 2013.
[2] D.G. McCartney, Grain refining of aluminium and its alloys using inoculants, Int. Mater. Rev. 34 (1989) 247–260, doi:10.1179/imr.1989.34.1.247.
[3] S. Jones, A.K. Prasada Rao, Z. Fan, Melt conditioned direct chill (MC-DC) casting of Al alloys, Trans. Indian Inst. Met. 66 (2013) 117–121, doi:10.1007/s12666-012-0235-5.
[4] H. Men, B. Jiang, Z. Fan, Mechanisms of grain refinement by intensive shearing of AZ91 alloy melt, Acta Mater. 58 (2010) 6526–6534, doi:10.1016/j.actamat.2010.08.016.
[5] M. Tong, J.B. Patel, I. Stone, Z. Fan, D.J. Browne, Identification of key liquid metal flow features in the physical conditioning of molten aluminium alloy with high shear processing, Comput. Mater. Sci. 131 (2017) 35–43, doi:10.1016/j.commatsci.2017.01.050.
[6] A. Dybalska, D.G. Eskin, J.B. Patel, Validation of the physical simulations of a stirred molten metal using particle image velocimetry data, JOM 70 (2018) 1256–1260, doi:10.1007/s11837-018-2924-y.
[7] L. Doucet, G. Ascanio, P.A. Tanguy, Hydrodynamics characterization of rotor-stator mixer with viscous fluids, Chem. Eng. Res. Des. 83 (2005) 1186–1195, doi:10.1205/cherd.04254.

[8] B. Jiang, Z. Fan, Grain initiation: progressive vs. explosive, in: Proceedings of the 6th Decennial International Conference on Solidification Processing, Old Windsor, UK, 2017, pp. 61–65.
[9] H.-T. Li, Y. Wang, Z. Fan, Mechanisms of enhanced heterogeneous nucleation during solidification in binary Al–Mg alloys, Acta Mater. 60 (2012) 1528–1537, doi:10.1016/j.actamat.2011.11.044.
[10] W.D. Bennon, F.P. Incropera, A continuum model for momentum, heat and species transport in binary solid-liquid phase change systems—I. Model formulation, Int. J. Heat Mass Transf. 30 (1987) 2161–2170, doi:10.1016/0017-9310(87)90094-9.
[11] C.J. Vreeman, M.J.M. Krane, F.P. Incropera, The effect of free-floating dendrites and convection on macrosegregation in direct chill cast aluminum alloys: part I: model development, Int. J. Heat Mass Transf. 43 (2000) 677–686, doi:10.1016/S0017-9310(99)00174-X.
[12] C.J. Vreeman, F.P. Incropera, The effect of free-floating dendrites and convection on macrosegregation in direct chill cast aluminum alloys: part II: predictions for Al–Cu and Al–Mg alloys, Int. J. Heat Mass Transf. 43 (2000) 687–704, doi:10.1016/S0017-9310(99)00175-1.
[13] C.J. Vreeman, J.D. Schloz, M.J.M. Krane, Direct chill casting of aluminum alloys: modeling and experiments on industrial scale ingots, J. Heat Transf. 124 (2002) 947–953, doi:10.1115/1.1482089.
[14] A.J. Williams, T.N. Croft, M. Cross, Modeling of ingot development during the start-up phase of direct chill casting, Metall. Mater. Trans. B 34 (2003) 727–734, doi:10.1007/s11663-003-0042-9.
[15] J. Ni, C. Beckermann, A volume-averaged two-phase model for transport phenomena during solidification, Metall. Trans. B 22 (1991) 349–361, doi:10.1007/BF02651234.
[16] L. Heyvaert, M. Bedel, M. Založnik, H. Combeau, Modeling of the coupling of microstructure and macrosegregation in a direct chill cast Al-Cu billet, Metall. Mater. Trans. A 48 (2017) 4713–4734, doi:10.1007/s11661-017-4238-z.
[17] K.O. Tveito, A. Pakanati, M. M'Hamdi, H. Combeau, M. Založnik, A simplified three-phase model of equiaxed solidification for the prediction of microstructure and macrosegregation in castings, Metall. Mater. Trans. A (2018), doi:10.1007/s11661-018-4632-1.
[18] J. Zuidema, Modelling of Flow Phenomena During DC Casting, Technische Universiteit Delft, 2005.
[19] A.R. Baserinia, H. Ng, D.C. Weckman, M.A. Wells, S. Barker, M. Gallerneault, A simple model of the mold boundary condition in direct-chill (DC) casting of aluminum alloys, Metall. Mater. Trans. B 43 (2012) 887–901, doi:10.1007/s11663-012-9658-y.
[20] J.M. Reese, Characterization of the flow in the molten metal sump during direct chill aluminum casting, Metall. Mater. Trans. B 28 (1997) 491–499, doi:10.1007/s11663-997-0116-1.
[21] W.M. Rohsenow, J.P. Hartnett, Y.I. Cho (Eds.), Handbook of Heat Transfer, 3rd ed., McGraw-Hill, New York, 1998.
[22] A.T. Utomo, M. Baker, A.W. Pacek, Flow pattern, periodicity and energy dissipation in a batch rotor–stator mixer, Chem. Eng. Res. Des. 86 (2008) 1397–1409, doi:10.1016/j.cherd.2008.07.012.
[23] A.T. Utomo, Flow Patterns and Energy Dissipation Rates in Batch Rotor-Stator Mixers, The University of Birmingham, 2009.
[24] A. Utomo, M. Baker, A.W. Pacek, The effect of stator geometry on the flow pattern and energy dissipation rate in a rotor–stator mixer, Chem. Eng. Res. Des. 87 (2009) 533–542, doi:10.1016/j.cherd.2008.12.011.
[25] G.S.B. Lebon, G. Salloum-Abou-Jaoude, D. Eskin, I. Tzanakis, K. Pericleous, P. Jarry, Numerical modelling of acoustic streaming during the ultrasonic melt treatment of direct-chill (DC) casting, Ultrason. Sonochem. 54 (2019) 171–182, doi:10.1016/j.ultsonch.2019.02.002.
[26] Q. Le, S. Guo, Z. Zhao, J. Cui, X. Zhang, Numerical simulation of electromagnetic DC casting of magnesium alloys, J. Mater. Process. Technol. 183 (2007) 194–201, doi:10.1016/j.jmatprotec.2006.10.009.
[27] H. Zhang, H. Nagaumi, Y. Zuo, J. Cui, Coupled modeling of electromagnetic field, fluid flow, heat transfer and solidification during low frequency electromagnetic casting of 7XXX aluminum alloys, Mater. Sci. Eng. A 448 (2007) 189–203, doi:10.1016/j.msea.2006.10.062.
[28] V. Hatić, B. Mavrič, N. Košnik, B. Šarler, Simulation of direct chill casting under the influence of a low-frequency electromagnetic field, Appl. Math. Model. 54 (2018) 170–188, doi:10.1016/j.apm.2017.09.034.
[29] H.-T. Li, P. Zhao, R. Yang, J.B. Patel, X. Chen, Z. Fan, Grain refinement and improvement of solidification defects in direct-chill cast billets of A4032 alloy by melt conditioning, Metall. Mater. Trans. B 48 (2017) 2481–2492, doi:10.1007/s11663-017-1016-7.
[30] H.G. Weller, G. Tabor, H. Jasak, C. Fureby, A tensorial approach to computational continuum mechanics using object-oriented techniques, Comput. Phys. 12 (1998) 620, doi:10.1063/1.168744.
[31] M.X. Xia, A.K. Prasada Rao, Z.Y. Fan, Solidification mechanisms in melt conditioned direct chill (MC-DC) cast AZ31 billets, Mater. Sci. Forum. 765 (2013) 291–295, doi:10.4028/www.scientific.net/MSF.765.291.
[32] A. Dybalska, Understanding and Development of High Shear Technology for Liquid Metal Processing, Brunel University London, 2016 http://bura.brunel.ac.uk/handle/2438/14518.
[33] V.R. Voller, C. Prakash, A fixed grid numerical modeling methodology for convection-diffusion mushy region phase-change problems, Int. J. Heat Mass Transf. 30 (1987) 1709–1719, doi:10.1016/0017-9310(87)90317-6.
[34] C.R. Swaminathan, V.R. Voller, A general enthalpy method for modeling solidification processes, Metall. Trans. B 23 (1992) 651–664, doi:10.1007/BF02649725.
[35] J.A.J. Robinson, A.W.D. Hills, A.T. Dinsdale, R.F. Brooks, L.A. Chapman, B. Roebuck, P.N. Quested, Prediction of properties of steels relevant to process simulation, in: Proceedings of European Conference on Thermophysical Properties, Bratislava, 2005, p. 73.
[36] J.A.J. Robinson, R.F. Brooks, P.N. Quested, Prediction of properties of metals relevant to process simulation, High Temp. Mater. Process. (2012) 31, doi:10.1515/htmp-2012-0031.
[37] A.B. Metzner, Rheology of suspensions in polymeric liquids, J. Rheol. 29 (1985) 739–775, doi:10.1122/1.549808.
[38] A. Yoshizawa, Statistical theory for compressible turbulent shear flows, with the application to subgrid modeling, Phys. Fluids 29 (1986) 2152, doi:10.1063/1.865552.
[39] S.L. Yeoh, G. Papadakis, M. Yianneskis, Numerical simulation of turbulent flow characteristics in a stirred vessel using the les and rans approaches with the sliding/deforming mesh methodology, Chem. Eng. Res. Des. 82 (2004) 834–848, doi:10.1205/0263876041596751.
[40] J. Aubin, D.F. Fletcher, C. Xuereb, Modeling turbulent flow in stirred tanks with CFD: the influence of the modeling approach, turbulence model and numerical scheme, Exp. Therm. Fluid Sci. 28 (2004) 431–445, doi:10.1016/j.expthermflusci.2003.04.001.
[41] ProCAST, ESI Group, 2016.
[42] A. Miehe, U. Gross, Modelling of heat transfer and solidification processes in horizontal twin-roll casting of magnesium AZ31, IOP Conf. Ser. Mater. Sci. Eng. 33 (2012) 012017, doi:10.1088/1757-899X/33/1/012017.
[43] H.G. Weller, OpenFOAM, OpenCFD Ltd (ESI Group), 2018.
[44] G.F. Hewitt, Boiling, in: W.M. Rohsenow, J.P. Hartnett, Y.I. Cho (Eds.), Handbook of Heat Transfer, 3rd ed., McGraw-Hill, New York, 1998, p. 46.
[45] M. Faden, A. König-Haagen, S. Höhlein, D. Brüggemann, An implicit algorithm for melting and settling of phase change material inside macrocapsules, Int. J. Heat Mass Transf. 117 (2018) 757–767, doi:10.1016/j.ijheatmasstransfer.2017.10.033.
[46] K. Fezi, A. Plotkowski, M.J.M. Krane, Macrosegregation modeling during direct-chill casting of aluminum alloy 7050, Numer. Heat Transf. Part Appl. 70 (2016) 939–963, doi:10.1080/10407782.2016.1214508.
[47] Q. Du, D.G. Eskin, L. Katgerman, Modeling macrosegregation during direct-chill casting of multicomponent aluminum alloys, Metall. Mater. Trans. A 38 (2007) 180–189, doi:10.1007/s11661-006-9042-0.
[48] D.M. Stefanescu, Science and Engineering of Casting Solidification, Springer, Cham, 2015.
[49] H. Hao, D.M. Maijer, M.A. Wells, A. Phillion, S.L. Cockcroft, Modeling the stress-strain behavior and hot tearing during direct chill casting of an AZ31 magnesium billet, Metall. Mater. Trans. A 41 (2010) 2067–2077, doi:10.1007/s11661-010-0216-4.
[50] A. Hadadzadeh, M.A. Wells, Mathematical modeling of thermo-mechanical behavior of strip during twin roll casting of an AZ31 magnesium alloy, J. Magnes. Alloys 1 (2013) 101–114, doi:10.1016/j.jma.2013.04.001.
[51] F. Menter, T. Esch, Elements of industrial heat transfer predictions, in: Proceedings of the 16th Brazilian Congress of Mechanical Engineering, Uberlândia, Brazil, 2001, pp. 117–127.